Electronic Supplementary Material (ESI) for Green Chemistry.

Supporting Information

Unprecedented catalytic performance in amines syntheses via Pd/g-C_3N_4 catalyst– assisted transfer hydrogenation

Xingliang Xu, Jiajun Luo, Liping Li, Dan Zhang, Yan Wang and Guangshe Li*

State Key Laboratory of Inorganic Synthesis and Preparative Chemistry, College of Chemistry, Jilin University, Changchun 130012, P. R. China

*Corresponding author: Guangshe Li; Tel.: +86 431 85168358

E-mail address: guangshe@jlu.edu.cn

Table of Contents

1 EXPERIMENTAL SECTION

Chemicals

All chemicals were purchased from commercial sources and used without further treatment. Formic acid (FA, 99 %), THF (99.8 %), and nitro- and aldehyde-compounds were purchased from Sigma-Aldrich. Palladium chloride ($PdCl_2$, 95 %) was purchased from Strem Chemicals, and cyclohexane (98.5%), DMF (100 %), ethanol (100 %) and toluene (98 %), $NaBH_4$ (98 %) from Fisher Scientific.

Characterization

X-ray diffraction patterns of the samples were obtained with a Rigaku D/max-2550 diffractometer using Cu Kα target (λ=0.154 nm). The step width is set at 0.02° with a scanning speed of 5°/min in a two theta range of 10 and 80°. High-resolution transmission electron microscopy (HRTEM) characterization was performed with a Tecnai F20 electromicroscope from FEI Company with an acceleration voltage of 200 KV. FT-IR spectra of the samples were recorded with KBr disks in the wavelength range of 400-4000 cm^{-1} using Bruker-IFS 66 V/S spectrophotometer combined with a gas Vacuum handling system. Adsorption-desorption isotherms of N_2 for the samples were measured using a TriStar 3000 (Micromeritics) nitrogen adsorption apparatus at 77 K. Brunauer-Emmett-Teller (BET) specific surface area and pore volume were calculated, respectively. X-ray photoelectron spectroscopy (XPS) data of the samples were acquired on a Thermo ESCALAB 250 spectrometer using Al Kα radiation (1486.6 eV) as X-ray source. Higher-resolution scans were recorded for the main core lines at pass energy of 20 eV. All peaks were calibrated using C1s core level at 284.6 eV.

The progress of the reaction and the yield of the amine compounds were determined

using TRACE DSQ GC−MS (Thermo Scientific Co, TR−wax−ms column 30.0 m ×320 μm×0.25 μm). Helium served as the carrier gas at a constant flow rate of 1.0 mL/min. The temperature program started at 60 ^{o}C for 1 min, then the temperature was increased from 60 to 150 ^{o}C at a rate of 10 ^{o}C /min, and subsequently increased from 150 to 250 ^{o}C at a rate of 20 ^{o}C /min. Ion source and transfer line temperatures were set at 250 and 240 ^{o}C, respectively. Mass spectrometric data were acquired and processed using GC-MS data system, and compounds were identified by gas chromatographic retention index and mass spectrum comparison with authentic standards, literature and library data, and unknown compounds were characterized by data comparison of the retention time dependent unknown compounds with those of standard compounds.

In the decomposition of formic acid reaction, the evolved gas was measured using a gas burette in real time at room temperature. The generated gas composition was qualitatively analysed by GC (Agilent GC-2014C equipped with a thermal conductivity detector).

2 Results

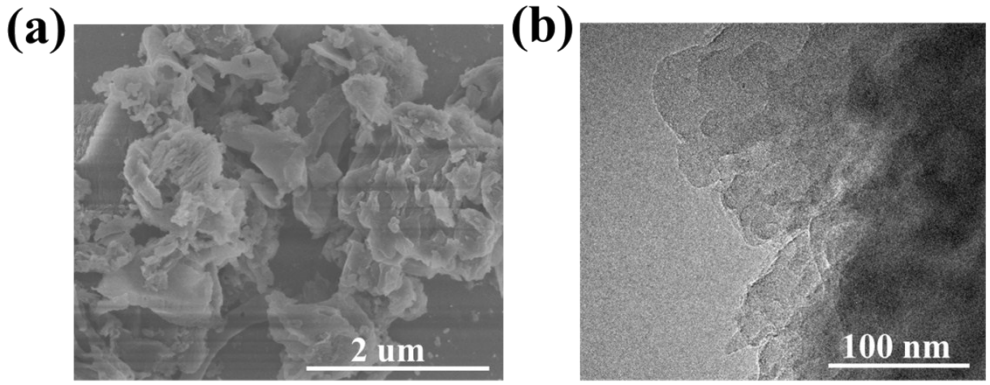

Fig. S1 (a) SEM and (b) TEM images of the as-synthesized g-C_3N_4.

Pure g-C_3N_4 shows sheet-like structure, and was a superior carrier for small-size noble metal loading.

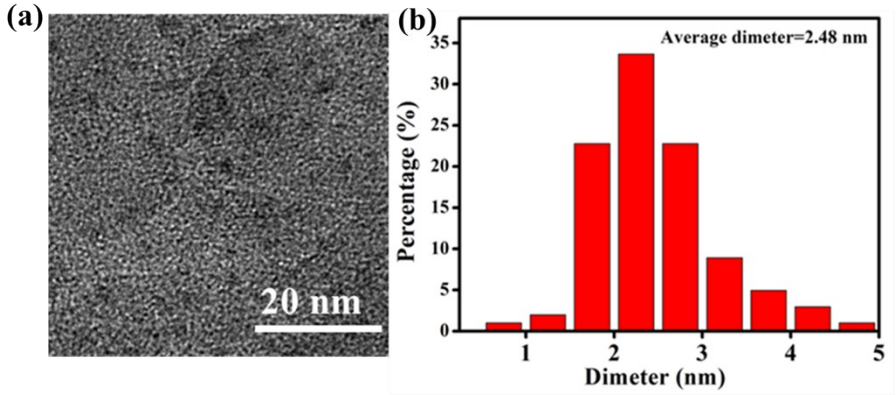

Fig. S2 (a) TEM image of 1 wt% Pd/g-C_3N_4 catalyst and (b) the size distribution of Pd nanoparticles.

TEM image of 1 wt% Pd/g-C_3N_4 sample shows that Pd NPs with an average particle size of 2.48 nm were distinctly anchored onto g-C_3N_4 nanosheets.

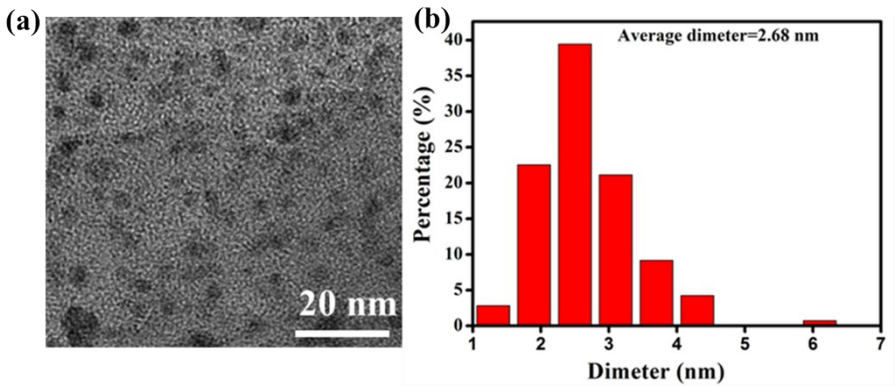

Fig. S3 (a) TEM image of 3 wt% Pd/g-C_3N_4 catalyst and (b) the size distribution of Pd nanoparticles.

When the Pd loading increased from 1 wt% to 3 wt%， TEM image of 3 wt% Pd/g-C_3N_4 sample shows that Pd NPs with an average particle size of 2.68 nm were distinctly anchored onto the g-C_3N_4 nanosheets.

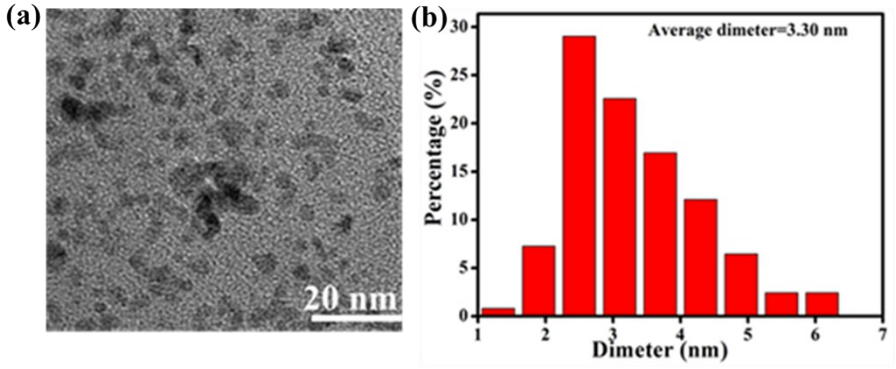

Fig. S4 (a)TEM image of 5 wt%Pd/g-C_3N_4 catalystand (b) the size distribution of Pd nanoparticles.

When the Pd loading is 5 wt %, TEM image of 5 wt% Pd/g-C_3N_4 sample shows that Pd NPs with an average particle size of 3.30 nm were distinctly anchored onto the g-C_3N_4 nanosheets.

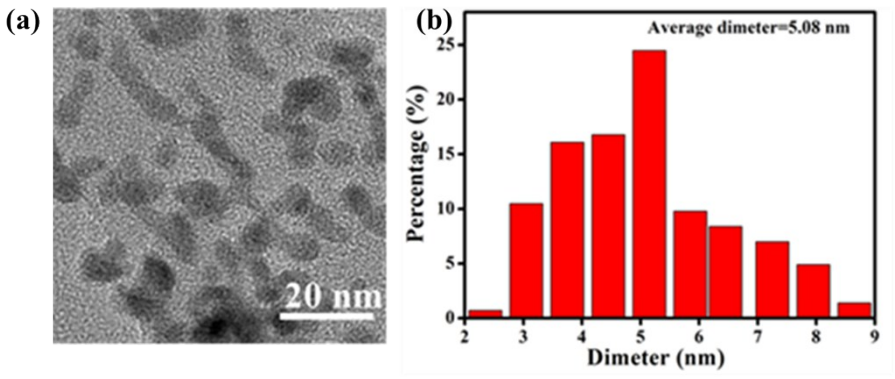

Fig. S5 (a)TEM image of 8 wt% Pd/g-C_3N_4 catalyst and (b) the size distribution of Pd nanoparticles.

When the Pd loading increased from 5 wt% to 8 wt%, the Pd NPs average particle size increased to 5.08 nm, and Pd NPs were distinctly anchored on the g-C_3N_4 nanosheets.

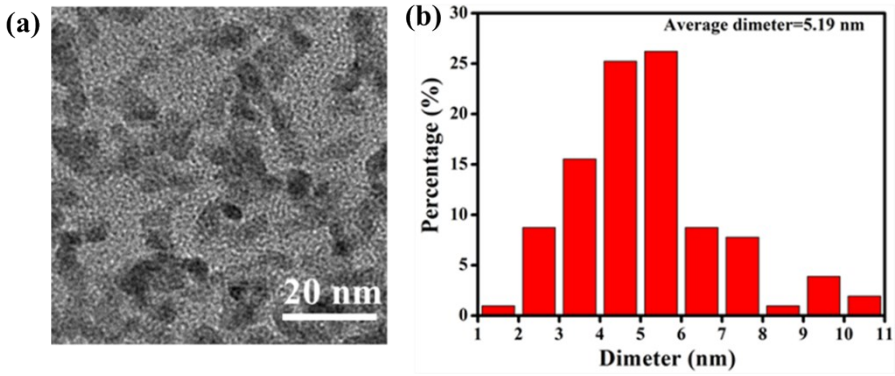

Fig. S6. (a)TEM image of 10 wt% Pd/g-C_3N_4 catalyst and (b) the size distribution of Pd nanoparticles.

When the Pd loading is 10 wt %, TEM image of 10 wt% Pd/g-C_3N_4 sample (Fig. S6) exhibits Pd NPs were distinctly anchored on the g-C_3N_4 nanosheets with an average particle size of 5.19 nm.

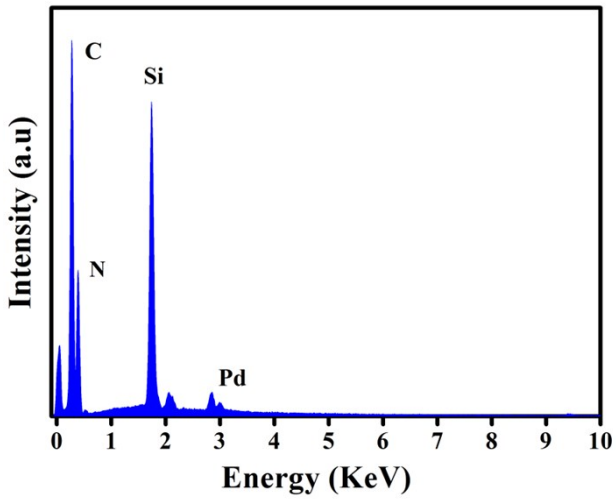

Fig. S7 EDX spectrum of 5 wt% Pd/g-C_3N_4 sample deposited on a silicon wafer. The spectrum shows peaks of C, N, Si, and Pd. Si peaks are from silicon wafer.

EDX results showd that C, N, O, and Pd elements coexisted in the 5 wt% Pd/g-C_3N_4, consistent with XPS results.

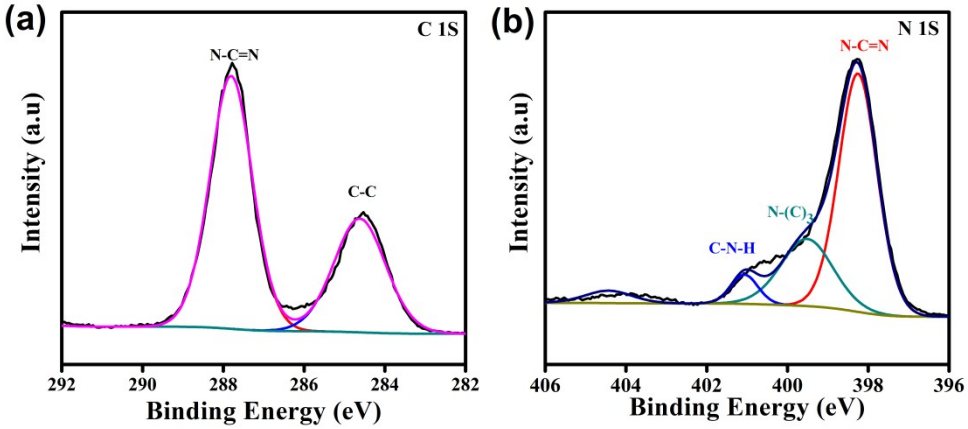

Fig. S8 XPS spectra of C1S (a)and N1s (b) spectra of g-C_3N_4.

From the high-resolution XPS spectra of C1s of g-C_3N_4, two main peaks at binding energies of 284.6 and 288.2 eV were attributed to graphitic carbon and C-N-C coordination in g-C_3N_4, respectively. In N1s spectrum (Figure S8b), three peaks at 398.3, 399.5 and 401.1 eV could be detected, assigned to N-C=N groups, tertiary nitrogen N-C_3 groups and the amino functions carrying hydrogen (C-N-H), respectively.

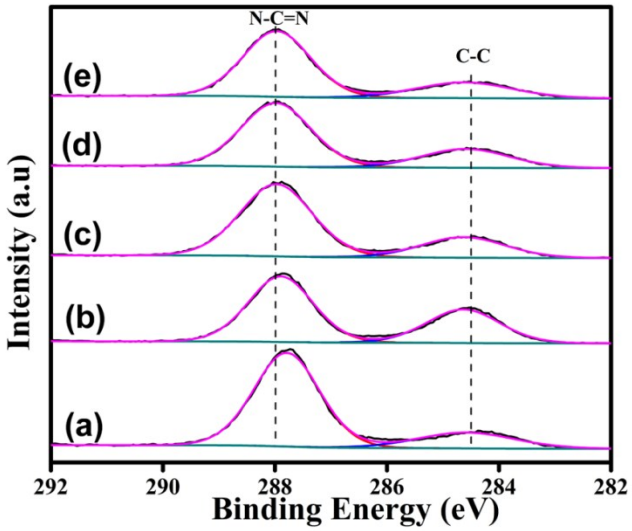

Fig. S9 XPS spectra of C 1S spectra of Pd/g-C_3N_4 with different of Pd loadings: (a) 1 wt%, (b) 3 wt%, (c) 5 wt%, (d) 8 wt%, and (e) 10 wt%.

All Pd/g-C_3N_4 samples have the characteristic C1S spectra in g-C_3N_4 with a higher binding energy, indicating the presence of strong interaction between support of g-C_3N_4 and Pd NPs with the increase of Pd loading.

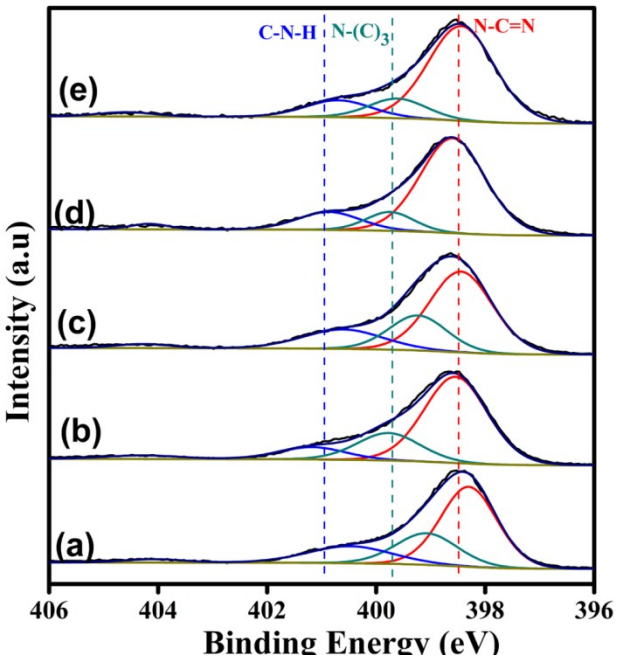

Fig. S10 XPS spectra of N 1S spectra of Pd/g-C_3N_4 with different of Pd loadings: (a) 1 wt%, (b) 3 wt%, (c) 5 wt%, (d) 8 wt%, (e) 10 wt%.

All Pd/g-C_3N_4 samples have the characteristic N1S spectra in g-C_3N_4 at a higher binding energy, indicating the presence of strong interaction between support of g-C_3N_4 and Pd

NPs with the increase of Pd loading.

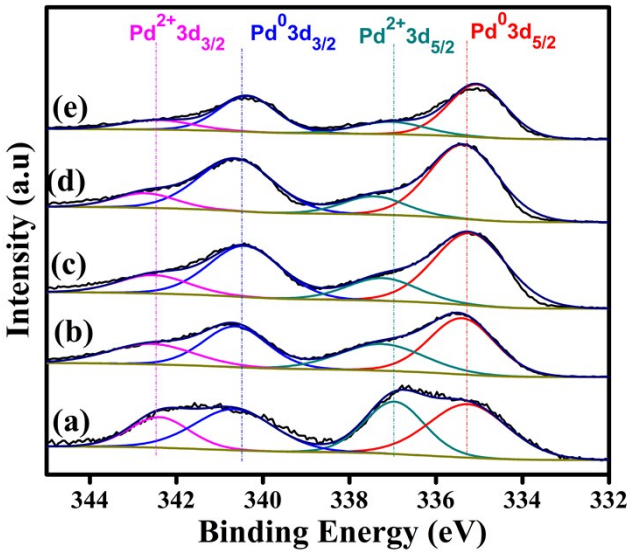

Fig. S11 XPS spectra of Pd 3d spectra of Pd/g-C_3N_4 with different of Pd loadings: (a) 1 wt%, (b) 3 wt%, (c) 5 wt%, (d) 8 wt%, (e)10 wt%.

XPS spectra of Pd 3d showed doublet peaks, corresponding to spin-orbital splitting of Pd $3d_{5/2}$ and Pd $3d_{3/2}$ for two types of Pd species. The stronger peaks at binding energies of 335.2-335.4 and 340.5-340.8 eV for Pd $3d_{5/2}$ and Pd $3d_{3/2}$ are from metallic Pd^0, and those with relatively low intensities at binding energies of 337.2-377.5 and 342.5-342.8 eV can be assigned to Pd^{2+}, which might be the formation of Pd-O or Pd-N bonds on the surface of catalyst. In addition, as seen from Table. S1, with the loading of Pd increasing (1 wt% to 5 wt%), the content of Pd^0 increases and then remains unchanged (Pd loading >5wt%).

Table S1 Physicochemical properties of the samples

Catalyst	Pd loading [wt%]	Particle size [nm]	Binding Energy of Pd^0 $Pd3d_{5/2}$ [eV]	Binding Energy of Pd^0 $Pd3d_{3/2}$ [eV]	Pd^0 [%]	BET [m^2/g]
g-C_3N_4						26.55
1 wt%Pd/ g-C_3N_4	0.98	2.48	335.3	340.7	63%	25.69
3 wt%Pd/ g-C_3N_4	2.97	2.68	335.4	340.6	67%	25.35
5 wt%Pd/ g-C_3N_4	4.98	3.30	335.2	340.5	75%	24.27
8 wt%Pd/ g-C_3N_4	7.96	5.08	335.4	340.8	74%	22.47
10 wt%Pd/ g-C_3N_4	9.97	5.19	335.2	340.5	75%	22.45

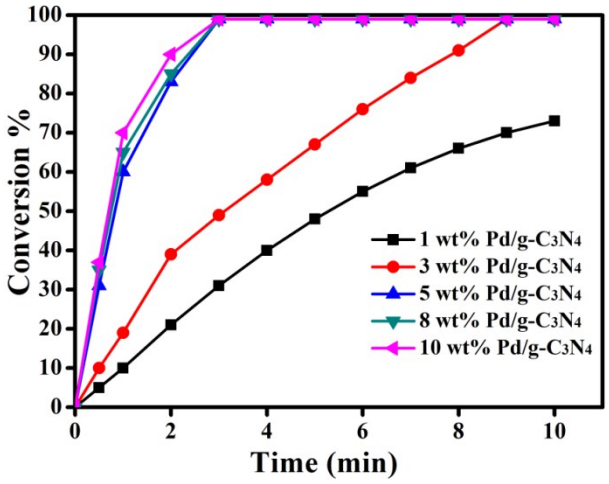

Fig. S12 Plot of time vs the conversion of nitrobenzene catalyzed by Pd/g-C_3N_4 with different Pd loadings. Reaction conditions: catalyst (20 mg), water (5 mL), nitrobenzene (1 mmol), FA (3 mmol), 298 K.

The reaction rate gradually increased with the increase of the Pd loading (Fig. S12). However, the turnover frequency (TOF) increased significantly to a maximum of 3172 min^{-1} at the Pd loading of 5%, and then slightly decreased when continuously increasing Pd loading to 8% and 10% (Fig. S13). Considering the atom utilization, we chose 5 wt% Pd/g-C_3N_4 as the optimum catalyst.

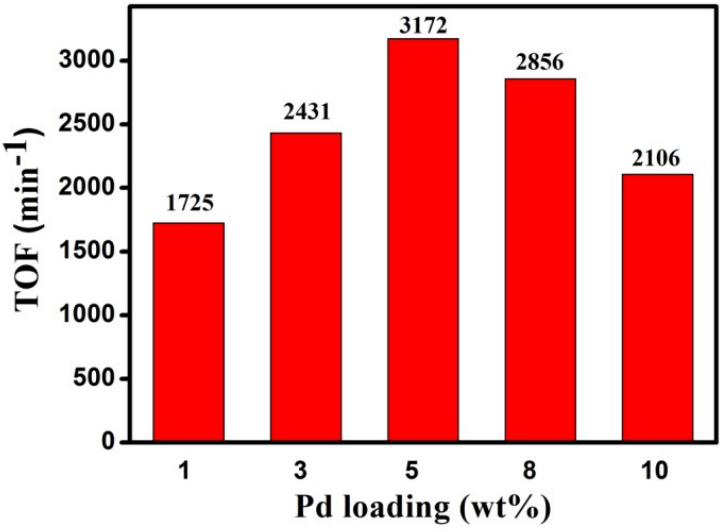

Fig. S13 Activity of Pd/g-C_3N_4 catalysts with different of Pd loadings for nitrobenzene reduction. Reaction conditions: catalyst (20 mg), water (5 mL), nitrobenzene (1 mmol), FA (3 mmol), 298 K.

The turnover frequency (TOF) is based on the amount of Pd atoms in catalysts, which is calculated from the equation below:

$$TOF = \frac{n_a}{n_{Pd} \cdot t}$$

Where n_a is the yield of amines (mol), n_{Pd} is the total moles of Pd in catalysts, t is the completion time of the reaction in hour. The initial TOF was calculated based on the aniline yield level at 1 min.

Table S2. TOF values for conversion of nitrobenzene catalyzed by various catalysts

Catalyst	H-donor	Solvent	T (K)	TOF (h^{-1})	Reference
5 wt% Pd/g-C_3N_4	HCOOH	Water	298	3172	This work
PVP-Pd NPs	$NaBH_4$	EtOH-H_2O	298	960	S1
Pd	H_2	MeOH	323	258	S2
Pd/Fe_2O_3	H_2	EtOH	298	48.5	S3
Pd/C (NF)	H_2	AcOEt	298	815	S4
Pd-Si (foam)	H_2	AcOEt	298	120[a]	S5
Ps-Pd-MgO	PMHS	H_2O	353	30[a]	S6
Pd-SS	$NaBH_4$	MeOH- H_2O	323	60[a]	S7
Pd-Fe/Al_2O_3	MeOH	H_2O	393	2.4	S8
Pd_9Ag_1-*N*-doped-MOF-C	HCOOH	EtOH-H_2O	303	396	S9
Fe/PP_3	HCOOH	EtOH	343	24.8	S10
5 wt% Pd/g-C3N4	$N_2H_4 \cdot H_2O$	EtOH	343	106	S11

[a]Reduction of *p*-chloronitrobenzene

Table S3. Catalytic transfer hydrogenation of various nitro compounds and various aldehydes to secondary amines [a].

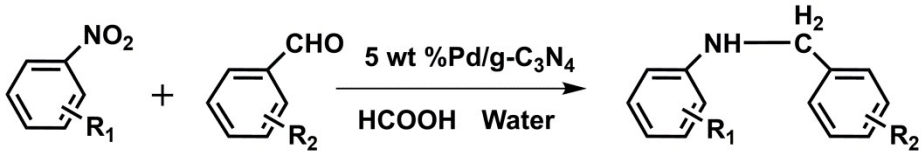

Entry	R1	R2	Temperature [°C]	Time [h]	Con.[b] [%]	Sel.[b] [%]
1	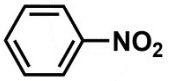	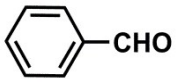	100	12	99	95
2	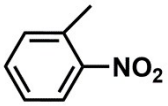	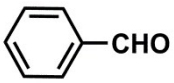	100	12	99	92
3	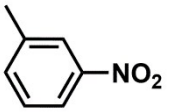	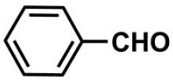	100	12	99	94
4	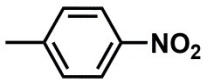	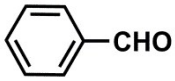	100	12	99	91
5	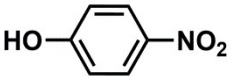	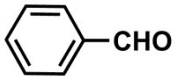	140	12	99	90
6	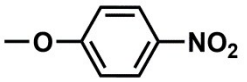	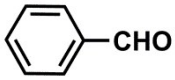	120	12	99	95
7	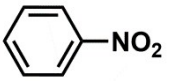	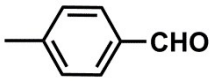	120	20	90	92
8	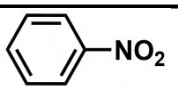	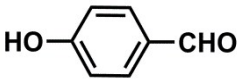	140	15	91	94
9	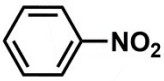	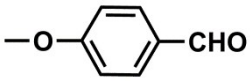	140	13	93	94

[a] Reaction conditions: 5 wt% Pd/g-C_3N_4 (2 mol%), water (5 mL), nitro compounds (1 mmol), aldehydes (1.5 mmol) FA (4.5 mmol),. [b] Conversions [Con.] and selectivity [Sel.] were determined by GC-MS.

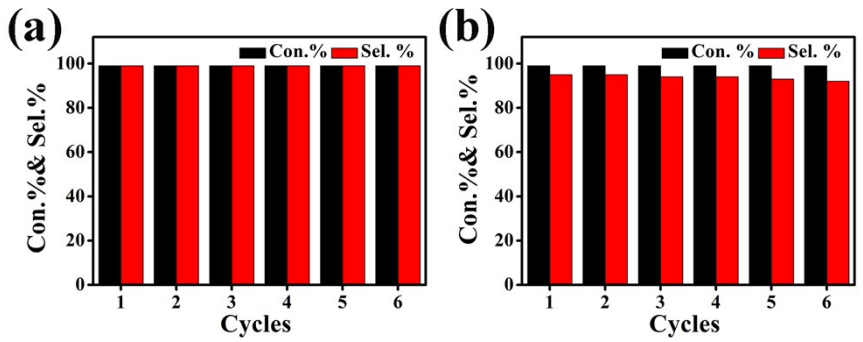

Fig. S14 Reuse of 5 wt% Pd/C_3N_4 (a) for nitrobenzene reduction and (b) for the reductive amination of benzaldehyde with nitrobenzene. Reaction conditions: (a)5 wt% Pd/C_3N_4 (1 mol%), water (5 mL), nitrobenzene (1 mmol), FA (3 mmol), 298 K; (b) 5 wt%Pd/g-C_3N_4 (2 % mol), benzaldehyde (1.5 mmol), nitrobenzene (1 mmol), water (5 mL), HCOOH (4.5 mmol) and time (12 h), 373 K

The reusability performance of catalyst is an important property for representing its stability. The catalyst was recycled at least six times without considerable change in conversion of nitrobenzene, and the selectivity toward aniline was all above 99% (Fig. S14a). For the reductive amination of benzaldehyde with nitrobenzene reaction, no considerable change in conversion of nitrobenzene (the conversions were ranging from 99% to 97% after 12 h) was observed. Moreover, the selectivity toward N-benzylaniline was all above 92% (Fig. S14b), suggesting that this catalyst has an excellent reusability.

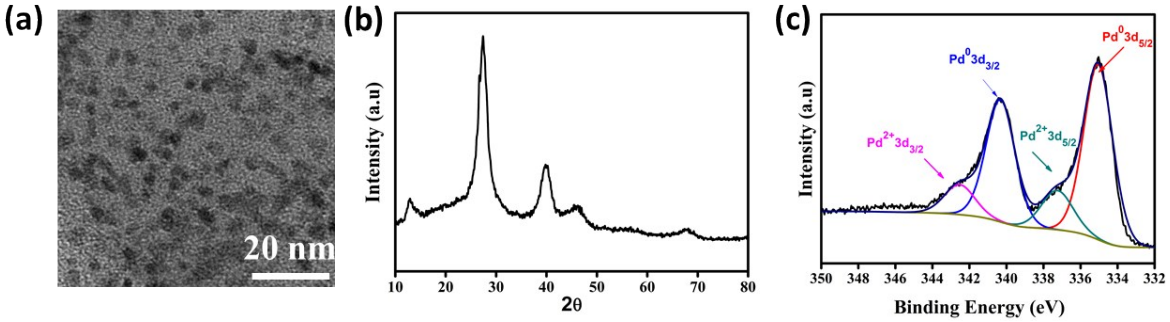

Fig. S15 (a) TEM image, (b) XRD pattern, and (c) Pd3d core level photoelectron spectra of 5 wt% Pd/C_3N_4 after 6 runs for the reductive amination of benzaldehyde with nitrobenzene.

TEM images taken for the 5 wt% Pd/g-C_3N_4 catalyst after the fifth catalytic cycle did not show obvious change in morphology (Fig. S15 a). The XRD patterns and XPS spectra (Fig. S15 b, c) show that the structure and the valence state of 5 wt% Pd/g-C_3N_4 catalyst after six runs are almost the same, confirming a high stability and reusability of 5 wt% Pd/g-C_3N_4 catalyst under reaction conditions.

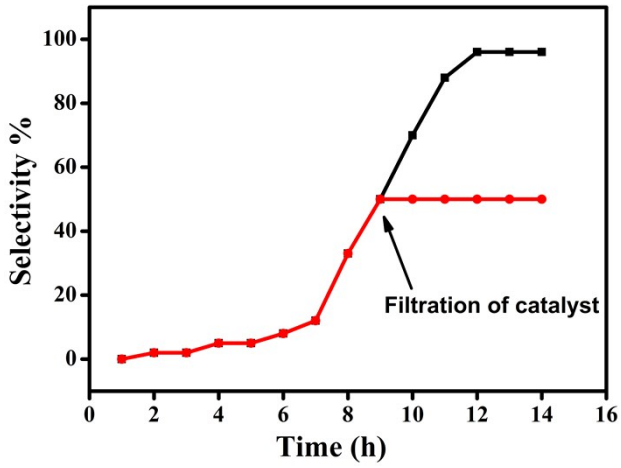

Fig. S16 Hot filtration test of the reductive amination of benzaldehyde with nitrobenzene. Reaction conditions: 5 wt% Pd/g-C_3N_4 (2 % mol), benzaldehyde (1.5 mmol), nitrobenzene (1 mmol), water (5 mL), HCOOH (4.5 mmol) and time (12 h). The catalyst was filtered after 9 h at 100 °C.

A hot-filtration test was carried out to verify the heterogeneous nature of the reaction (Fig. S16). After removal of the solid catalyst at 9 h, no reaction proceeded in the filtrate. These results indicate that the catalytic effect in this system results from the current sample, rather than the leached metal species.

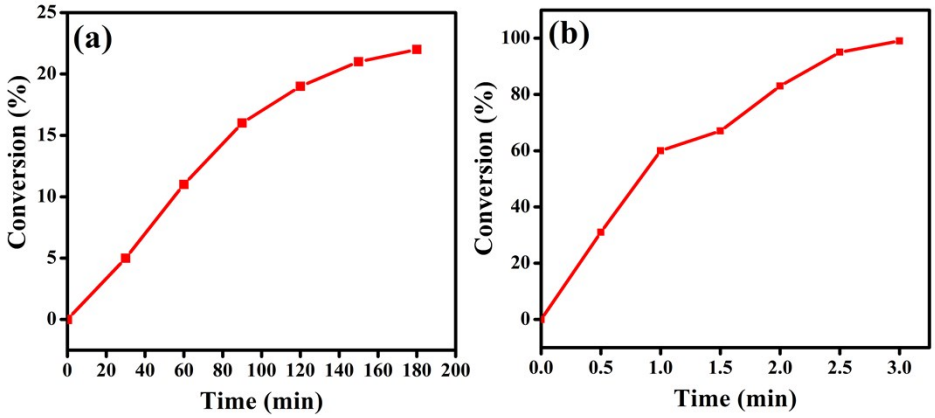

Fig. S17 Plots of time vs the conversion of FA catalyzed by 5 wt% Pd/g-C_3N_4: (a) without and (b) with nitrobenzene (1 mmol). Reaction conditions: 5 wt%Pd/g-C_3N_4 (20 mg), water (5 mL), FA (3 mmol), 298 K.

In order to compare the reaction rate of formic acid catalytic transfer hydrogenation and the rate of formic acid decomposition, we studied the conversion of formic acid with nitrobenzen and without nitrobenzen (Fig. S17). It can be seen from Fig. S17a that the decomposition rate of

formic acid is very low in the absence of nitrobenzene. After 3 hours, only 20% of formic acid was decomposed. However, after the addition of nitrobenzene, the utilization of formic acid has been significantly improved. In 3 minutes, formic acid can achieve 100% utilization (Fig. S17b).

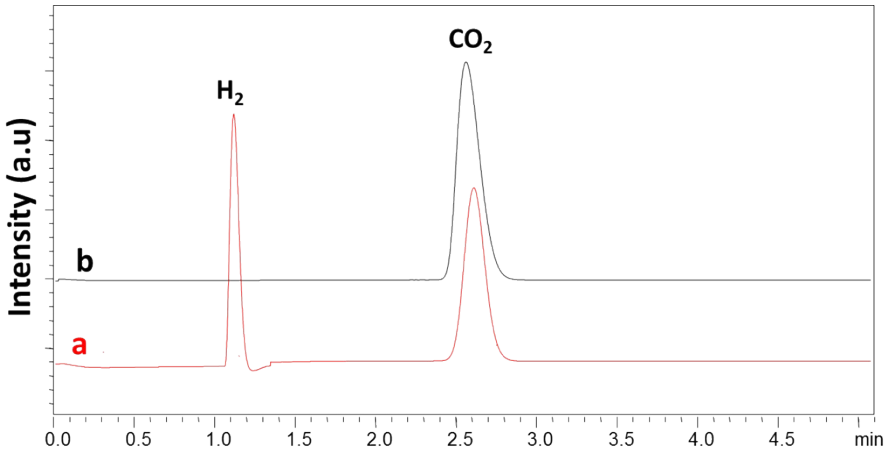

Fig. S18 GC spectra for the gas evolved from the dehydrogenation of FA (a) without and (b) with nitrobenzene over 5 wt% Pd /g-C_3N_4.

In order to explore the mechanism of reaction, we studied the decomposition of formic acid. The generated gas composition was qualitatively analyzed by GC. The hydrogen and carbon dioxide are detected in the decomposition of formic acid reaction (Fig S18a). What's more, the hydrogen was not observed in the presence of nitrobenzene (Fig S18b), which indicates that the catalytic transfer hydrogenation reaction is preferred in the presence of nitrobenzene.

3 Mass spectrogram of some amines (10 largest peaks based on EI)

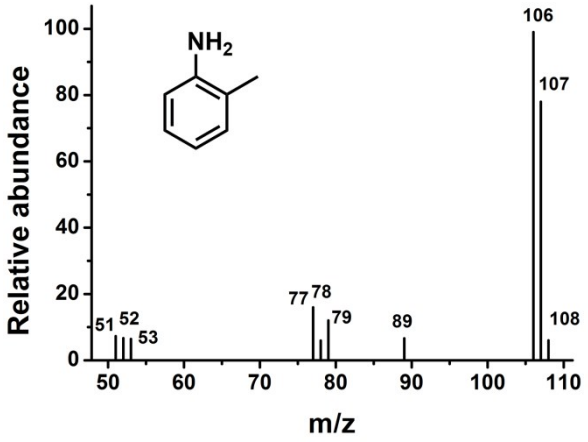

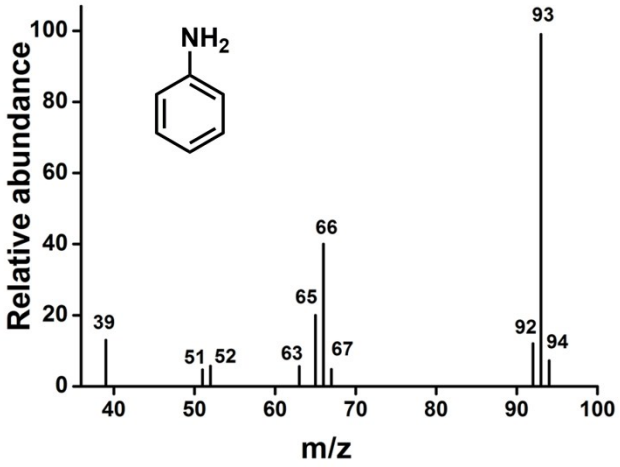
NH2
Relative abundance
m/z
93
66
65
39
92
94
51
52
63
67

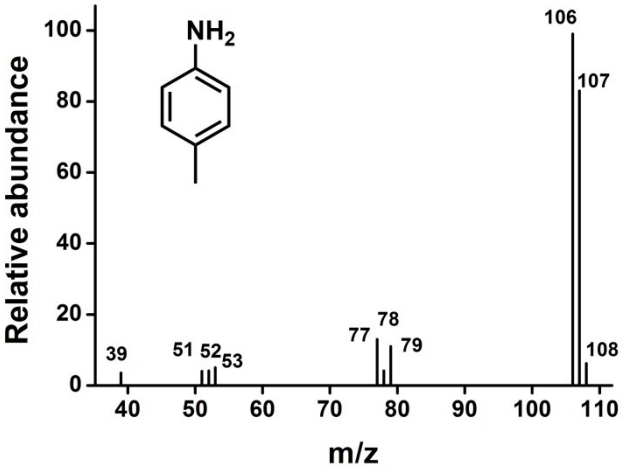
NH2
Relative abundance
m/z
106
107
78
77
79
39
51
52
53
108

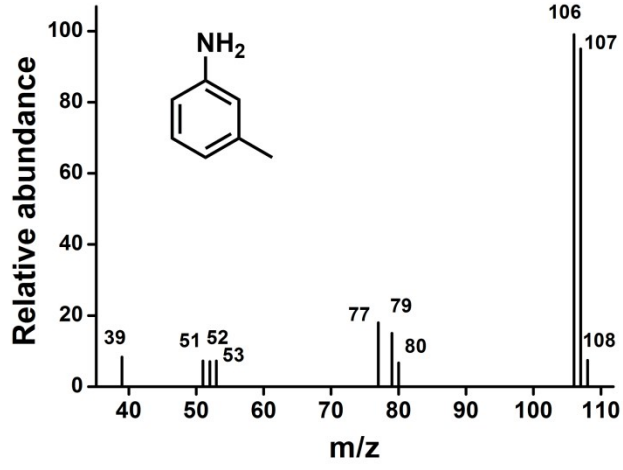
NH2
Relative abundance
m/z
106
107
77
79
80
39
51
52
53
108

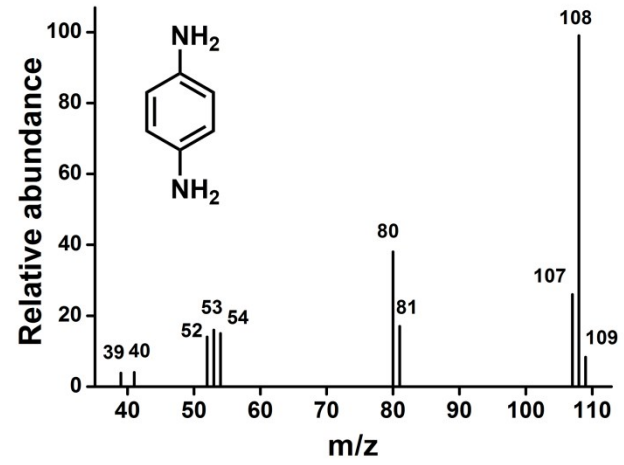
NH2
NH2
Relative abundance
m/z
108
80
107
81
53
54
52
109
39 40

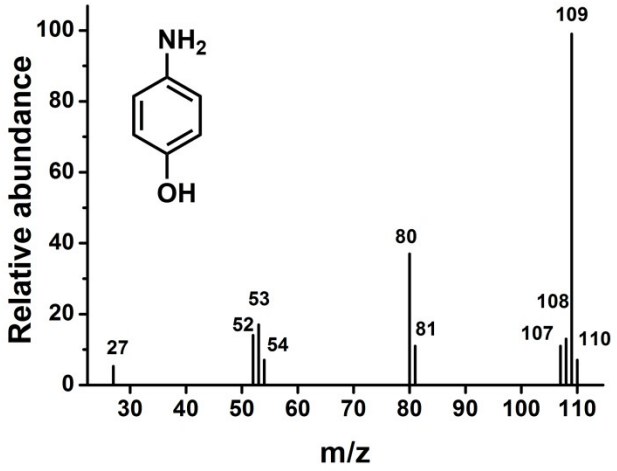
NH2
OH
Relative abundance
m/z
109
80
53
52
108
107
81
54
110
27

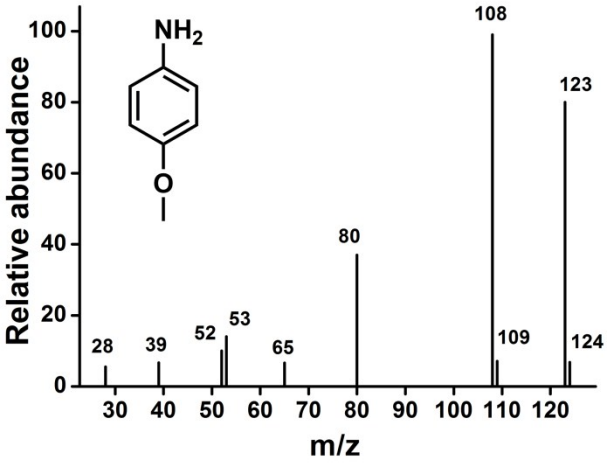
NH2
O
Relative abundance
m/z
108
123
80
53
52
109
124
65
28
39

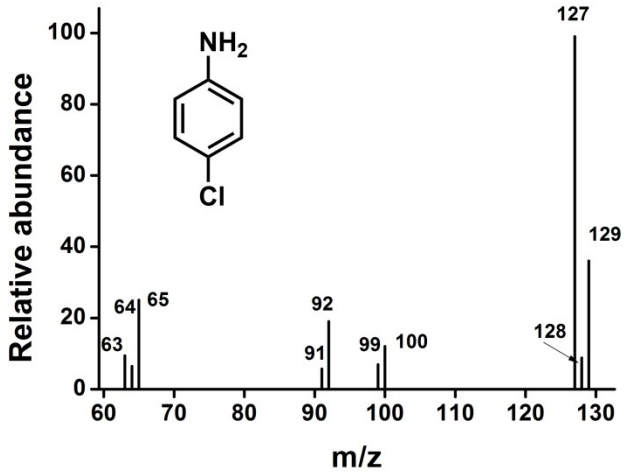
NH2
Cl
Relative abundance
m/z
127
129
128
92
65
64
63
91
99
100

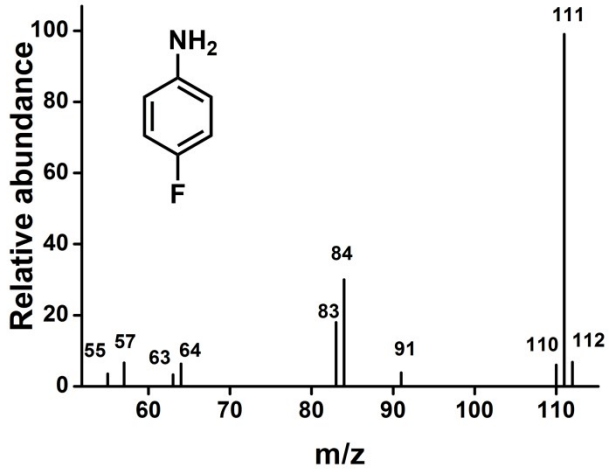
NH2
F
Relative abundance
m/z
111
84
83
55
57
63
64
91
110
112

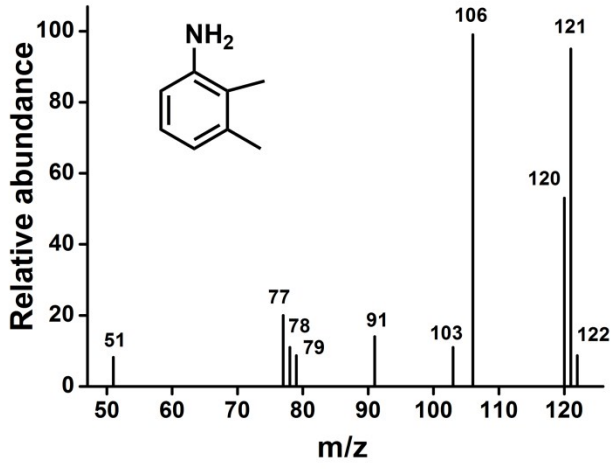
NH2
Relative abundance
m/z
106
121
120
77
78
79
91
103
122
51

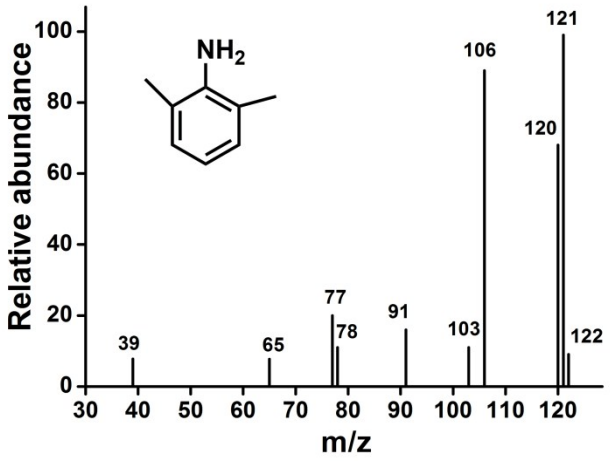

References

S1 P. M. Uberman, C. S. Garca, J. R. Rodrguez, S. E. Martn, *Green Chem.,* 2017, **19,** 739–748.

S2 N. Arai, N. Onodera, A. Dekita, J. Hori and T. Ohkuma, *Tetrahedron Lett.,* 2015, 56, 3913-3915

S3 A. J. Amali and R. K. Rana, *Green Chem.,* 2009, **11,** 1781-1786.

S4 M. Takasaki, Y. Motoyama, K. Higashi, S. H. Yoon, I. Mochida and H. Nagashima, *Org. Lett.,* 2008, **10,** 1601-1604.

S5 O. Verho, K. P. J. Gustafson, A. Nagendiran and C. Tai, *ChemCatChem,* 2014, **6,** 3153-3159

S6 D. Damodara, R. Arundhathi, T. V. Ramesh Babu, M. K. Legan, H. J. Kumpaty and P. R. Likhar, *RSC Adv.*, 2014, **4,** 22567-22574

S7 K. Shil, D. Sharma, N. R. Guha and P. Das, Tetrahedron Lett., 2012, **53,** 4858-4861.

S8 Y. Z.Xiang, X. N. Li, C. S. Lu, L . Ma, and Q. F. Zhang, *Appl. Catal. A-Gen.* 2010, **375,** 289-294

S9 Z. Liu，W .H. Dong, S. S. Cheng, S. Guo, N. Z. Shang, S. T. Gao, C. Feng, C. Wang and Z.Wang, *Cataly. Commun.,* 2017, **95,** 50-53.

S10 K. J. Datta, A. K. Rathi, M. B. Gawande, V. Ranc, G. Zoppellaro, R. S. Varma and Radek Zboril, *ChemCatChem*. 2016, **8,** 2351 -2355.

S11 D. Nandi, S. Siwal, M. Choudhary and K. Mallick, Appl. Catal. A-Gen. 2016, 523, 31-38.